RESEARCH ARTICLE

Probing the growth of β-FeSi$_2$ nanoparticles for photovoltaic applications: a combined imaging and spectroscopy study using transmission electron microscopy

A. S. W. Wong[1]*, G. W. Ho[2], S. L. Liew[1], K. C. Chua[1] and D. Z. Chi[1]

[1] Institute of Materials Research and Engineering—3 Research Link, Singapore 117602

[2] National University of Singapore—Electrical and Computer Engineering, Singapore

ABSTRACT

The microstructure of β-FeSi$_2$ nanoparticles grown using magnetron sputtering on Si has been examined using various electron microscopy techniques. FeSi$_2$ nanoparticles as small as ∼4 nm are found embedded in Si after growth using co-sputtering of FeSi$_2$ and Si, followed by rapid thermal annealing (RTA). The formation of nanoparticles and its variation in density with Fe content is discussed in terms of phase separation. Our study shows that the size and density of the nanoparticles as well as the extent of Fe diffusion into sputtered Si and substrate can be controlled by controlling the Fe content in the co-sputtered film. Copyright © 2011 John Wiley & Sons, Ltd.

1. INTRODUCTION

β-Iron disilicide (β-FeSi$_2$) has a direct band gap of 0.80–0.85 eV and a high optical adsorption coefficient of 10^5/cm^2 at 1 eV [1,2]. It is present in abundance in the earth crust resulting in low material cost and is considered to be a more environmentally friendly compared to materials like CIGS and CdTe. All these make β-FeSi$_2$ a desirable candidate for photovoltaic and light emitting applications [3–6]. Although the theoretical energy conversion efficiency for this material is 16–23% [7–10], the highest laboratory-based result reported so far is 3.7% at 100 mW/cm^2 which is preceded by 0.35% at 100 mW/cm^2 [11]. Significant increase in cell efficiency from 0.35 to 3.7% was attributed to the fabrication of high quality epitaxial β-FeSi$_2$ films by introducing a thin β-FeSi$_2$ template layer pre-formed on Si(111) substrates at 400°C, followed by annealing at 600°C [12]. In addition, the template layer also acts as a blocking layer for Fe diffusion into Si(111) substrate during high temperature annealing [12]. Fe introduces defect levels in Si, which can act as traps for photo-generated carriers thereby reducing solar cell efficiency [13,14]. Thus, it is clear that there is a growing imperative to solve technical issues, both in materials and in cell design/architecture, in order to close up the differences between the experimental and theoretical energy conversion efficiencies.

β-FeSi$_2$ films can be grown by a variety of techniques such as facing target sputtering (FTS) [12–14] and molecular beam epitaxy (MBE) [15–18]. β-FeSi$_2$ can also be grown using magnetron sputtering, a cheaper and faster alternative to MBE, either by depositing Fe on Si substrate, or by depositing FeSi$_2$ directly onto any substrate, both followed by thermal annealing. The former approach involves the solid state reaction between Fe and Si substrate and can result in rough surface and interfaces [19–21], whilst the latter has the flexibility of deposition on non-Si substrates such as glass and steel [22]. Here, we attempt to grow nanoparticles embedded in Si to enhance solar cell efficiencies. It has also been reported that the formation of β-FeSi$_2$ nanoparticles in Si can introduce strain in β-FeSi$_2$ nanoparticles which modifies band structure from indirect to direct band gap, thereby improving room temperature

electroluminescence [23,24]. β-FeSi$_2$ nanoparticles formation has been reported using ion beam synthesis [25,26] and reactive deposition epitaxy [27]. In the former, Fe is implanted with a dose of 5×10^{15} cm^{-2} into Si, followed by rapid thermal annealing (RTA) at 900°C to precipitate out β-FeSi$_2$ nanoparticles. In the latter, Fe was first deposited on Si at 470°C, forming a 15 nm thick β-FeSi$_2$, which agglomerates into islands upon further annealing at 850°C for 1 h. These nanostructures are subsequently capped with a layer of sputtered Si. Both approaches require high temperature and long time furnace annealing, resulting in Si dislocations which affects electroluminescence [25,26]. In addition, 5 nm diameter strained FeSi$_2$ nanodots were epitaxially grown on Si(111) using Fe and Si co-deposition via electron beam evaporation at 500°C [28]. Unfortunately, this technique is limited to growth of FeSi$_2$ nanodots on Si(111) substrates and diffusion of Fe into Si at elevated growth temperatures remains unknown. More recently, Terasawa *et al.* [29] fabricated FeSi$_2$/Si composite films by alternate deposition of FeSi$_2$ and Si onto quartz substrate and subsequent annealed the films using scanning annealing. Terasawa *et al.* [29], however, did not study Fe diffusion into the sputtered Si on nanometer-scale nor did the author addressed the issues of crystallization of a-Si in these films. The motivation of our work stems from our believe that, with a nano-structured Si film embedded with β-FeSi$_2$ nanoparticles, we can take the combined advantages of high optical absorption of semiconducting β-FeSi$_2$ and good carrier transport ability of Si (μe ~1500 and μh ~450 cm^2/V-s at 300 K) to fabricate high energy conversion efficiency solar cells with a much reduced film thickness (compared to Si thin film solar cells). For FeSi$_2$ nanoparticles embedded in Si matrix formed using magnetron sputtering and RTA annealing, it remains unclear what factors are most important in affecting nanoparticle formation in terms of nanoparticle size, density and Fe diffusion into Si. In this paper, we prepared various nanoparticle films by varying the sputtering and post-sputtering annealing conditions, and studied these effects on the films using various electron microscopy techniques.

In addition, apart from work done by Liu *et al.* [11,12], who showed that Fe diffusion can be effectively suppressed using a template layer, no similar work has been carried out in sputtered films. Given that the presence of Fe in Si can be detrimental to performance of future solar cells with this architecture [13,14], we strongly believe that the matter of Fe diffusion has to be studied and resolved before any useful devices can be made using these films. In this paper, we sputtered a thick Si layer between the Si substrate and the nanoparticle film and study the effect of annealing on Fe diffusion.

2. EXPERIMENTAL

Si(100) substrates were cleaned in dilute hydrofluoric acid (1%) to remove native oxides. Films deposition was performed in a Denton sputtering system equipped with two DC and one RF sputtering cathode and a sample

rotation stage to ensure uniform deposition. The FeSi2 and Si targets were mounted onto DC and RF cathodes, respectively. Cleaned Si substrates were placed into a sputtering chamber and pumped to a base pressure of 5×10^{-7} Torr before argon gas was flow at a rate of 25 sccm. With this Ar gas flow rate, a working pressure of 3×10^{-3} Torr was maintained throughout the deposition process. The FeSi$_2$ and Si targets were pre-sputtered for 10 min with the shutter closed to remove any oxides and/or organic contaminants that may be present on the targets. FeSi$_2$ and Si films were deposited directly onto DHF-cleaned Si(100) by DC sputtering. Post-deposition annealing was carried out using an RTA system in nitrogen at 500–800°C for 60 s. After annealing, the films were cooled to room temperature over a period of 20 min before the chamber was vented and samples removed. FeSi$_2$ nanoparticles embedded in Si were formed by first depositing Si (first layer) onto Si(100) substrate, followed by co-sputtering of FeSi$_2$ and Si (second layer) and finally depositing another layer of Si (third) onto the second layer. For the second layer, the Si power was kept at 100 W whilst the FeSi$_2$ power was varied from 10 to 100 W. For the multi-layer samples, three Si/FeSi$_2$ + Si/Si repeating structures were grown. Post-deposition annealing was carried out in nitrogen at 600–800°C for 60 s.

The sample morphologies were determined using a JEOL JSM 6700 field emission scanning electron microscope (SEM) system operating in the secondary electron mode at 5 kV. Transmission electron microscopy (TEM) specimens were prepared using conventional grinding, polishing and dimpling. Electron transparent regions were obtained using a GATAN precision ion polishing system. Ar$^+$ milling was carried out with top and bottom incident gun angles of 8° at 5 keV, and finishing at 4–5° at 3–3.5 keV to minimize specimen damage. Film thicknesses, film/substrate interfaces and nanostructures were studied using cross-sectional transmission electron
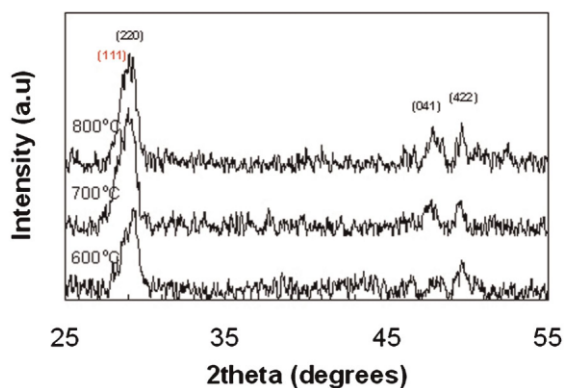
Figure 1. X-ray diffraction patterns of multi-layer sample with alternating sputtered Si and co-sputtered (Si and FeSi$_2$) layers annealed from 600 to 800°C. This structure is designed to produce FeSi$_2$ nanoparticles embedded in Si matrix. The black indices represents the β-FeSi$_2$ phases present whilst the red index is the Si(111) phase.

microscopy (XTEM) in a Philips CM300 TEM system equipped with a field emission electron source operated at 300 kV and an extractor voltage of 3.81 kV. Energy filtering TEM was carried out by aligning the zero loss peak and tuning the Gatan Imaging Filter (GIF). Scanning TEM (STEM) energy dispersive X-ray (EDX) analysis was carried out using a JEOL 2100 TEM operated at 200 kV and a FEI M-STEM system at 80 kV. The accelerating voltage was set at 80 kV to minimize sample damage due to high accelerating voltage. For STEM analysis, a 1-nm electron probe and an EDAX X-ray detector allows elemental quantification of nanometer-sized regions. In addition, high angle annular dark field imaging (HAADF) using a HAADF detector can also provide qualitative information on mean atomic number variation in films as large atoms scatters electron more strongly than small atoms. In HAADF bright contrast in these images suggest the

presence of large atoms, assuming that film thickness does not change across the analysed area. Phase identification was also carried out using X-ray diffraction from a general area detector diffraction system (GADDS) operated at 40 kV and 40 mA.

3. RESULTS AND DISCUSSION

Sun *et al*. [30] reported on the formation of high quality, dislocation-free β-FeSi$_2$ nanoparticles using ion beam synthesis in combination with RTA. Here, we study the effect of sputtering power in magnetron sputtering and RTA temperature on density and quality of the β-FeSi2 nanoparticles.

We prepared three co-sputtered layers sandwiched between four Si layers (100 W Si) on Si substrate, in an
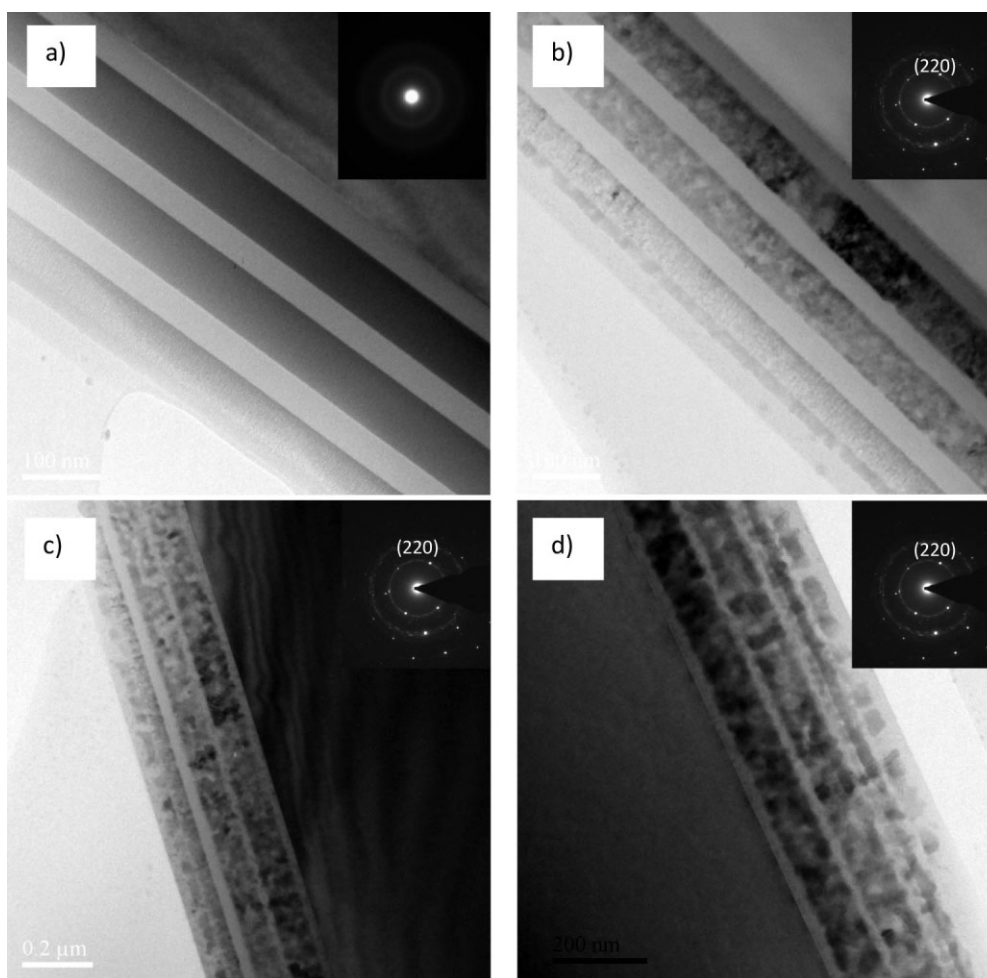
Figure 2. (a–d) Bright field TEM images of the multi-layer sample (a) as-deposited (b) 600°C, (c) 700°C, and (d) 800°C. The contrast in each layers in (a) is uniform, and together with the SAED pattern, confirms the sample to be amorphous. (b–d) At 600–800°C annealing, the contrast in the co-sputtered layer changes significantly, suggesting the formation of crystals with different orientation and/or composition. The weaker polycrystalline ring is indexed as the FeSi$_2$ (220). The single crystal spots are that of Si. The four inner spots are the (111) and the two outer spots are the (200) The sputtered Si layer appears to have reduced thickness at 800°C, likely due to the intermixing of Fe with Si.

attempt to grow FeSi$_2$ nanoparticles embedded within Si. The structure and the sputtering power used are as follows:

XRD diffraction patterns of the multi-layer structure show the presence of β-FeSi$_2$(220) peak, which confirms

$$Sisubstrate/Si(100W)/FeSi_2(100W) + Si(100W)/Si(100W)/FeSi_2(100W)\ldots$$
$$+Si(100W)/Si(100W)/FeSi_2(100W) + Si(100W)/Si(100W).$$

β-FeSi$_2$ formation at 600–800°C (Figure 1). Another peak with 2θ position very close to the FeSi$_2$(220) peak, attributed to the presence of Si(111), is also observed. In a separate study (results not presented here), pure sputtered Si films annealed between 600 and 700°C did not yield any Si(111) diffraction peaks. The Si(111) peak appears only at 800°C. Raman spectroscopy (data not presented here) of pure Si layers shows the same trend. This contrasts with the XRD study of the co-sputtered layers which confirms the presence of crystalline Si at 600C which suggests that the presence of FeSi$_2$ (in the co-sputtered film) may have lowered the crystallization temperature of the Si.

Figure 2a–d are bright field TEM images showing the nanostructural evolution with annealing temperature. The thickness of Si and co-sputtered layers in as-deposited films are 38 and 73 nm (Figure 2a), respectively. Uniform diffraction contrast and selected area diffraction patterns (SAED) taken from the layers confirm the as-deposited films to be amorphous (see inset). At 600–800°C, diffraction contrast and SAED patterns (innermost poly-crystalline ring is indexed as FeSi$_2$ (220)) within the co-sputtered clearly reveal the polycrystalline nature of the film. It is possible but difficult to observe the nanoparticles possibly due to large particle sizes and high nanoparticle density, causing overlapping of nanoparticles in cross-section.

STEM EDX analysis of the as-deposited co-sputtered layer (not presented here) yield 22 at% Fe and 78 at% Si, confirming the layer to be in Si-rich condition. The Si layers consist predominantly Si, with up to 5 at% O present in the films. HAADF imaging (Figure 3a) of the annealed co-sputtered films show non-uniform contrast within the co-sputtered layers, which confirms compositional difference within the layers. STEM EDX analysis (Figure 3b,c) of the films annealed at 800°C confirmed the film to consist of regions which are Si-rich (95 at% Si, 5 at% Fe), suggesting that phase separation has occurred during annealing.

It is also observed that the interface between Si and co-sputtered layers becomes more diffused with annealing temperature. STEM EDX analyses of the Si layers annealed at 600°C show the presence of 2–4 at% Fe in the first layer of Si and up to 17 at% in the second layer of Si. For a given temperature, the higher Fe content in the second Si layer can be due to the diffusion of Fe from the first and second co-sputtered layers, whilst Fe from the first Si layer originates only from the first co-sputtered layer. Conceivably, if the FeSi$_2$ target is stoichiometric, any

additional Si from co-sputtering will result in excess Si instead of Fe so the presence of Fe in the Si layer does suggests that Fe diffuses rapidly into the Si layers during annealing, before any silicidation can occur.
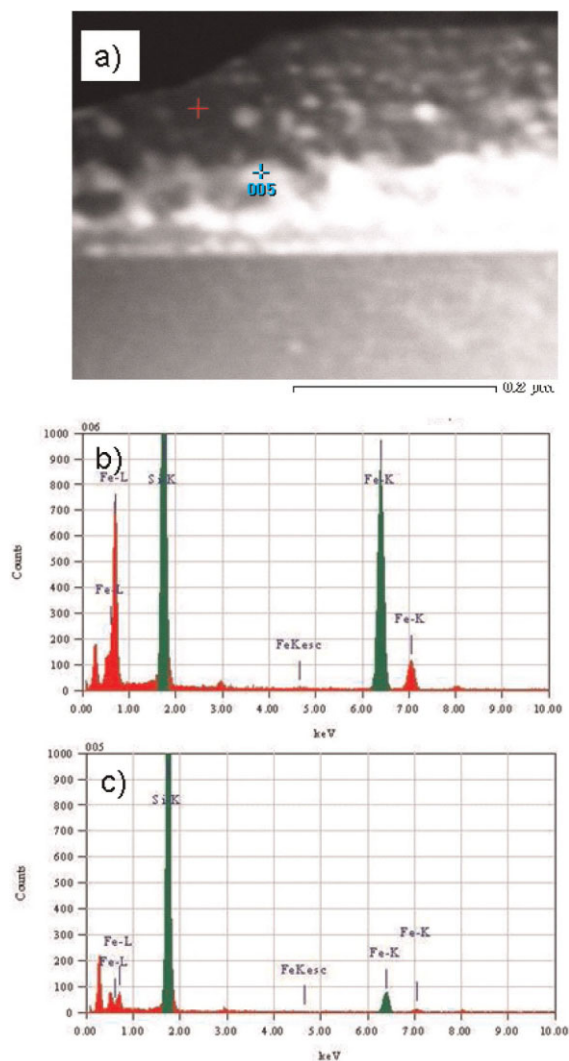
Figure 3. (a) HAADF images of as-deposited multi-layer sample. The edge of the sample is a hole in the TEM sample and appears completely black in the HAADF image. The co-sputtered layer consists of Fe and Si, and has the brightest contrast in the image. (b) STEM EDX analysis of all layers indicates trace amounts of O in the film (Layer 1). The co-sputtered layer (blue marker) consists of 22 at% Fe and 78 at% Si. (c) The corresponding EDX spectra of the region marked in red shows it to be predominantly Si, with (95 at% Si, 5 at% Fe).

Having shown that rapid Fe diffusion results in intermixing with Si layer, we considered finally the effects of Fe to Si ratio on nanoparticle formation. We studied the effect of Fe content in the films by varying the $FeSi_2$ target sputtering power from 50 W (first cosputtered layer from the bottom) to 10 W (third co-sputtered layer), whilst keeping the Si target power at 100 W. That is, three co-sputtered layers were grown between four Si layers in this order from the substrate Si substrate:

$$+Si(100W)/FeSi_2(10W) + Si(100W)/Si(100W).$$

Similarly, two XRD peaks are observed in the annealed samples. As illustrated in Figure 4a, the variation in the nanoparticles density with $FeSi_2$ power is clearly evident, with the 10 W yielding the lowest particle density and the nanoparticles are clearly distinguishable. A crystalline layer whose thickness increases with annealing temperature is observed at the sputtered Si/c-Si substrate interface (Figure 4b). At 800°C (Figure 4c), greater intermixing due to diffusion of Si and Fe causes interfacial roughening

between the layers, although the first co-sputtered layer still have stronger diffraction contrast due to the presence of more Fe from the $FeSi_2$ phase. Figure 4d clearly shows a distinct nanoparticle from the second cosputtered layer.

HAADF imaging of the multi-layers annealed at 600°C shows non-uniform contrast throughout the co-sputtered layers. The brightest contrast in the HAADF image is observed for the first co-sputtered layer due to highest concentration of Fe present. The Fe:Si ratio of the first, second and third co-sputtered ($FeSi_2 + Si$) layers determined using STEM EDX are on average 20: 80, 10: 90, 5:95, respectively, although it should be noted that trace amounts of O up to 5.5 at% observed in these layers are neglected in the quantification of the film composition. The low Fe concentration is due to low $FeSi_2$ nanoparticle density and the presence of excess Si through the specimen thickness analysed by STEM EDX. STEM EDX analysis of the sputtered first, second and third Si layers to have 4, 1.5 and 0 at% Fe, respectively. This clearly demonstrates that it is possible to limit Fe diffusion into the sputtered Si
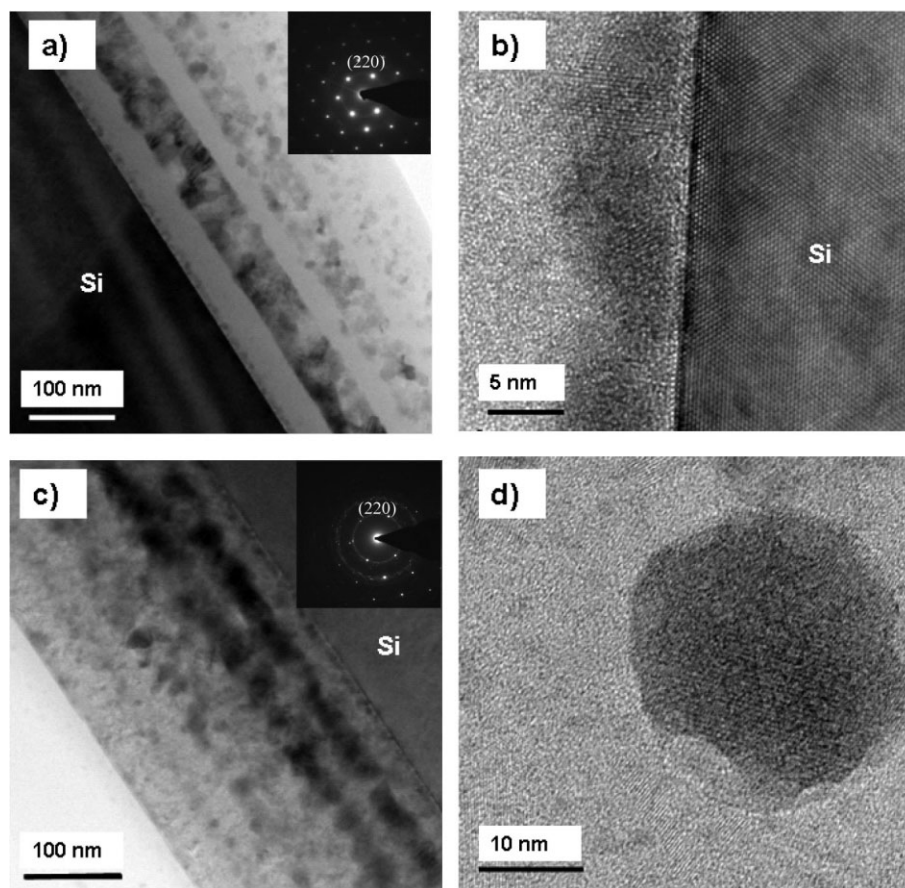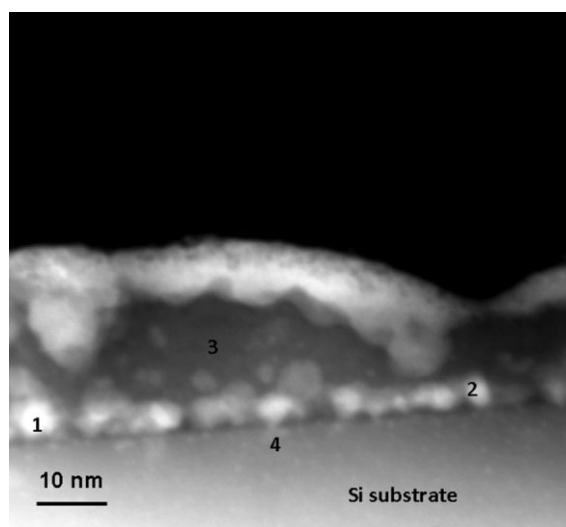

Figure 4. TEM images of multi-layer (varying power) samples annealed at 700°C. (a) Clearly shows the variation in nanoparticle density with $FeSi_2$ sputtering power. Inset shows the diffraction pattern taken from the film and substrate. The weaker polycrystalline ring is indexed as the $FeSi_2$ (220). The single crystal spots are that of Si. The four inner spots are the (111) and the two outer spots are the (200). (b) is a HRTEM image of the interfacial region. The dark contrast and the fringes within indicate the presence of a crystalline phase with a different composition from the sputtered Si. (c) illustrates the intermixing of the sputtered Si and co-sputtered layers at 800°C. (d) clearly shows a nanoparticle embedded within Si.

by minimizing the amount of Fe in the co-sputtered layers. The absence of Fe in the third Si layer suggests that all Fe present is consumed during silicidation to form $FeSi_2$. It also suggests that the rate of diffusion of Fe into the Si layer is dependent on the concentration of Fe atoms.

In a more detail study of the same sample, the HAADF image (Figure 5) of the sample annealed at 800°C first sputtered Si layer (closest to the Si substrate) shows non-uniform image contrast suggesting the composition variation at the interface. STEM EDX of Point 1 and 2 (Figure 5) image yields 16.32 at% Fe, 80.0 at% Si, 3.68 at% O and 6.07 at% Fe, 89.17 at% Si, 4.76 at% O, respectively. At point 3 and several others, we can also observe pure Si regions. Most importantly, no Fe (within the detection limit of this technique) is detected in the Si substrate close to the interface (point 4), suggesting that Fe has diffused to the interface to react with Si and O forming a Si-Fe-O compound. This is desirable as Fe diffusion into Si substrate introduces defect levels that degrade the performance of a solar cell device [11]. Previously, Liu *et al.* [11] successfully blocked the diffusion of Fe into Si via the growth of template layer ε-FeSi followed by two-step annealing process at 400°C and later 600°C to form the β-FeSi$_2$ phase. In addition, the rate of Fe diffusion in the sputtered Si may be different from the c-Si substrate. This shows that the presence of a sputtered Si layer can also effectively prevents Fe from diffusing into the Si substrate.

Figure 6a–f shows a series of energy-filtered dark-field TEM images taken for nanoparticles formed using 10W $FeSi_2$. Imaging was performed at 0.32° dark-field tilt and rotated from 0 to 360° around the bright field spot (hollow cone technique) which allows the imaging of d-spacing ~0.352 nm. The dark-field images provide insight into

Figure 5. High magnification HAADF image of the multi-layer (varying power) sample annealed at 800°C, 60 s. Non-uniform image contrast is attributed to compositional difference. STEM EDX analysis was performed at various positions marked 1–5.

the crystalline nature of the nanoparticles as they clearly show that different nanoparticles diffract strongly under different diffracting conditions. The Si substrate is observed to be non-diffracting in (a–e), as opposed to (f). Figure 6g illustrates the nanoparticle size distribution (determined from BFTEM and HAADF imaging) of the various layers after a annealing at 600°C. The average nanoparticle size for the first, second and third co-sputtered layers, determined from various bright-field and HAADF images, are ~30.8, 22.4 and 8.9 nm. Clearly, this study demonstrates that the nanoparticle size can be controlled by the Fe/Si ratio.

The physical principle of our approach which involves the co-sputtering of $FeSi_2$ and Si, is based on the thermodynamic argument that, within Si–Fe binary system, due to the line compound nature of $FeSi_2$, a phase separation of $FeSi_2$ from Si matrix will take place during thermal annealing process, if the Si/Fe ratio in the starting amorphous Si-Fe composite is much larger than the stoichiometric value 2 of $FeSi_2$. At annealing temperature between 600 and 900°C, solid state reaction results in the following reaction:

$$Fe + Si(excess) \rightarrow FeSi_2(nanoparticles) + Si(matrix)$$
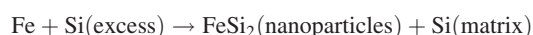
The mechanism of forming β-FeSi$_2$ nanoparticles by sputtering and then RTA in this study may have involved two processes. The first process is the diffusion of the Fe and Si species. The as-deposited film is amorphous and high temperature annealing results in the diffusion of Fe and Si species. Interestingly, the presence of Fe in the Si layers after annealing does suggest that the Fe from the Si-rich co-sputtered layers can diffuse rapidly into the sputtered Si layers, which actually happens before any crystallization can occur. At high Fe concentration (50 W $FeSi_2$), Fe is present in the first and second co-sputtered layers. In addition, the Fe diffused to the c-Si/sputtered Si interface to form a Si-Fe-O compound. As the concentration of Fe decreases (10 W $FeSi_2$), Fe diffusion is suppressed and pure sputtered Si layers can be obtained.

The second process is the crystallization of $FeSi_2$. The crystallization process is evident from the XRD results (Figure 1), which illustrates a broad peak due to the convolution of the $FeSi_2$ (220) and Si(111) peaks. The process of $FeSi_2$ and Si crystallization is observed to occur between 600 and 800°C. In our work, we did not anneal the films at >800°C as this may result in the formation of the tetragonal α-FeSi$_2$ with metallic property [29]. It has been reported that the crystallization temperature of a-Si can be affected by the heating rate and the a-Si particle size [31]. Although the Si(111) is observed, it is possible that there is still some a-Si in the film. For thick a-Si film, the crystallization temperature is observed to vary between 680 and 720°C, the higher Si crystallization temperature in our films is attributed to higher heating rate so a slower heating rate may ensure complete crystallization of Si. A similar observation is made in a-Si nanoparticles. For nanoparticles, it is reported that crystallization temperature increases with heating rate and decreasing particle size. For
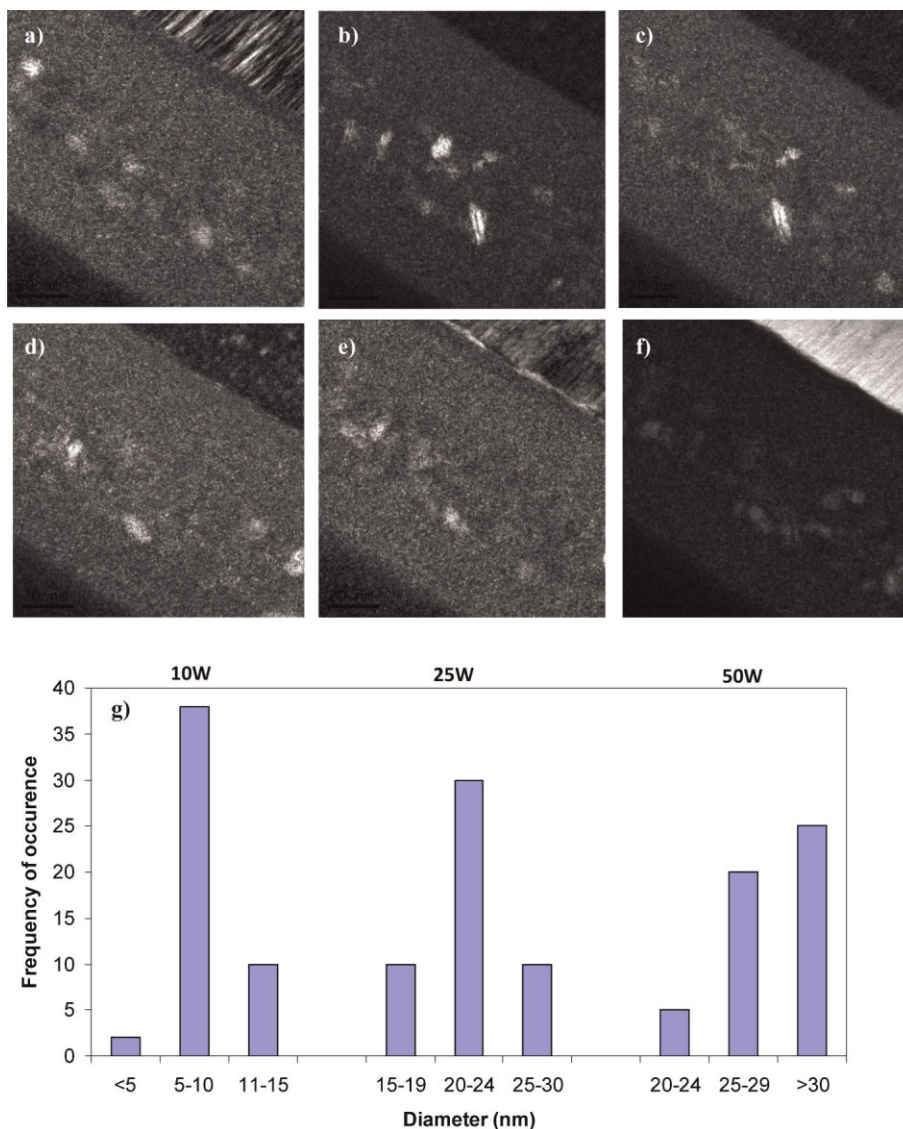
Figure 6. Energy-filtered dark-field TEM images of FeSi$_2$ nanoparticles embedded in sputtered Si. (a–f) show the nanoparticles to be diffracting at 0.32° tilt and rotated between 0 and 360° around the bright-field spot. (f) shows the substrate to be more strongly diffracting than the nanoparticles. (g) size distribution of the first, second and third co-sputtered layer with average nanoparticle size of $\sim$30.8, 22.4 and 8.9 nm, respectively.

particles $\sim$120 nm in diameter, crystallization temperature varies from 770 to 800°C. For smaller $\sim$40 nm particles, crystallization temperature can vary from 830 to 860°C [31]. However, the maximum annealing temperature is limited by the formation of α-FeSi$_2$ at higher temperatures so it is difficult to achieve β-FeSi$_2$ nanoparticles embedded in crystalline Si. Lastly, the precipitated or segregated FeSi$_2$ most likely form nano-particles within a Si layer with varying sizes depending on the Si/Fe. At the top co-sputtered layer grown using 10 W FeSi$_2$, crystalline and distinct nano-particles are observed (Figure 6h,i). Unlike implantation of Fe into Si [25,26], where ion dosage controls the amount of Fe incorporated into Si and for

which a low ion dose of 10^{15} cm^{-2} created particles of 20–40 nm, by controlling the target sputtering power, the smallest particle size reported here is $\sim$4 nm (Figure 6h). This contrasts with Teresawa *et al.* [29], in which the nanoparticle size varies from 10–35 to 30–50 nm, depending on the cycle time. In addition, no Si dislocations are observed for all the samples prepared using RTA. This observation is very similar to Sun *et al.* [30] who reported the absence of Si dislocations RTA samples. In their work, extended high-temperature annealing results in the formation of polygon-shaped nanoparticles, which is accompanied by the presence of dislocations at the β-FeSi$_2$/Si interface resulting in strain relief. It has been

determined that there exists 5% tensile strain in the $FeSi_2$ particle along the Si [111] direction [30].

4. CONCLUSION

Transmission electron microscopies systematically characterize the growth of $FeSi_2$ nanoparticles using magnetron sputtering and RTA. The formation mechanism of β-$FeSi_2$ nanoparticles was attributed to phase separation of $FeSi_2$ and Si grown under Si-rich condition. Sputtering power and post-deposition annealing are observed to affect $FeSi_2$ nanoparticle density. The amount of Fe in the co-sputtered films has been identified as the key factor in controlling and limiting nanoparticle size and achieving discrete $FeSi_2$ nanoparticles embedded in pure Si free from Fe. By reducing the Fe concentration in the films, we showed that it is possible to simultaneously grow smaller nanoparticles and suppress the diffusion of Fe into the sputtered Si layers and substrate.

ACKNOWLEDGEMENTS

REFERENCES

1. Bost MC, Mahan JE. Optical-properties of semiconducting iron disilicide thin films. *Journal of Applied Physics* 1985; **58**: 2696–2703.

2. Yamaguchi K, Mizushima K. Luminescent $FeSi_2$ crystal structures induced by heteroepitaxial stress on Si(111). *Physical Review Letters* 2001; **86**: 6006–6009.

3. Lefkl K, Muret P. Photoelectric study of β-$FeSi_2$ on silicon: optical threshold as a function of temperature. *Journal of Applied Physics* 1993; **74**: 1138–1142.

4. Wang SN, Otogawa N, Fukuzawa Y, Shen HL, Tanoue H, Kojima T, Nakayama Y, Makita Y. Prototype infrared optical sensor and solar cell made of beta-$FeSi_2$ thin film. *Proceedings of SPIE* 2003; **5065**: 188–195.

5. Nishida I. Study of semiconductor-to-metal transition in Mn-doped $FeSi_2$. *Physical Review B* 1973; **B7**: 2710–2713.

6. Wang SN, Otogawa N, Fukuzawa Y, Suzuki Y, Ootsuka T, Liu ZX, Osamura M, Mise T, Nakayama Y, Tanoue H, Makita Y. *Proceedings of the 3rd World Conference on Photovoltaic Energy Conversion*, Oosaka, Japan, 2003; 46–49 (1 PC).

7. Bube RH. Photovoltaic Materials. Imperial College Press: Amsterdam, 1998; 3.

8. Powalla M, Herz K. Coevaporated think films of semiconducting beta-$FeSi_2$. *Applied Surface Science* 1993; **65/66**: 482–488.

9. Yang Z, Homewood KP, Finney MS, Harry MA, Reeson KJ. Optical absorption study of ion beam synthes-

10. Makita Y., *Proceedings of the First NREL Conference*. In McConnel RD (ed.), 1997; 3-3.

11. Liu ZX, Wang SN, Otogawa N, Suzuki Y, Osamura M, Fukuzawa Y, Ootsukaa T, Nakayamab Y, Tanoue H, Makita Y. A thin-film solar cell of high-quality β-$FeSi_2$/Si heterojunction prepared by sputtering. *Solar Energy Materials and Solar Cells* 2006; **90**: 276–282.

12. Liu ZX, Suzuki Y, Osamura M, Ootsuka T, Mise T, Kuroda R, Tanoue H, Makita Y, Wang SN, Fukuzawa Y, Otogawa N, Nakayama Y. Reduction of iron diffusion in silicon during the epitaxial growth of beta-$FeSi_2$ films by use of thin template buffer layers. *Journal of Applied Physics* 2004; **95**: 4019–4024.

13. Wunstel K, Wagner P. Interstitial iron and iron-acceptor pairs in silicon. *Applied Physics A: Solids Surface* 1982; **27**: 207–212.

14. Isobe T, Nakashima H, Hashimoto K. Diffusion coefficient of interstitial iron in silicon. *Japanese Journal of Applied Physics, Part 1* 1989; **28**: 1282–1283.

15. Makita Y. Novel features of photoluminescence spectra from acceptor-doped GaAs: Formation of acceptor-acceptor pair emissions and optical compensation effect. *Materials Science & Engineering* 1996; **R16**(6–8): 265–398.

16. Makita Y, Nakayama Y, Fukuzawa Y, Wang SN, Otogawa N, Liu ZX, Osamura M, Ootsuka T, Mise T, Tanoue YH. Formation of thin beta-$FeSi_2$ template layer for the epitaxial growth of thick film on Si(111) substrate. *Thin Solid Films* 2004; **461**: 34–39.

17. Wang SN, Otogawa N, Fukuzawa Y, Suzukiki Y, Ootsuka T, Osamura M, Mise T, Liu ZX, Tanoue H, Nakayama Y, Makita Y. Boron doping for p-type beta-FeSi2 films by sputtering method. *Japanese Journal of Applied Physics* 2004; **43**(4A): 504–506.

18. Ugajin Y, Sunohara T, Suemasu T. Investigation of current injection in beta- $FeSi_2$/Si double-hetero structures light-emitting diodes by molecular beam epitaxy. *Thin Solid Films* 2007; **515**: 8136–8139.

19. Nolan TP, Sinclair R. Modelling of agglomeration in polycrystalline thin films—Application to $TiSi_2$ on a silicon substrate. *Journal of Applied Physics* 1992; **71**: 720–724.

20. Wong ASW, Chi DZ, Loomans M, Ma D, Lai MY, Tjiu WC, Chua SJ, Ma D. F-enhanced morphological and thermal stability of NiSi films on BF_2^+-implanted Si(001). *Applied Physics Letters* 2002; **81**(27): 5138–5410.

21. Ma D, Chi DZ, Loomans ME, Wang WD, Wong ASW, Chua SJ. Kinetics of NiSi-to-NiSi2 transformation and morphological evolution in nickel silicide thin films on Si(001). *Acta Materialia* 2006; **54**(18): 4905–4911.

22. Liu ZX, Osamura M, Ootsuka T, Kuroda R, Makita Y, Tanoue H, Fukuzawa Y, Otogawa N, Nakayama Y. Formation of beta-FeSi2 thin films on non-

silicon substrates. *Thin Solid Films* 2006; **515**: 1532–1538.

23. Leong D, Harry M, Reeson KJ, Homewood KP. *Nature 387* 1997; **686**.

24. Suemasu T, Negishi Y, Takakura K, Hasegawa F. *Japanese Journal of Applied Physics 39* 2000; **L1013**.

25. Martinelli L, Grilli E, Guzzi M, Grimaldi MG. Room-temperature electroluminescence of ion-beam-synthesized beta-FeSi$_2$ precipitates in silicon. *Applied Physics Letters* 2003; **83**: 794–796.

26. Ishimaru M, Omae K, Bae It, Naito M, Hirotsu Y. Formation process of beta-FeSi$_2$/Si heterostructure in high-dose Fe ion implanted Si. *Journal of Applied Physics* 2006; **99**: 113527, 1–7.

27. Hsu HF, Wu HY, Huang YT, Chen TH. Structural properties of iron silicide nanostructures grown by reactive deposition epitaxy. *Japanese Journal of Applied Physics* 2009; **48**: 08JB09, 1–3.

28. Nakamura Y, Nagadomi Y, Cho SP, Ichikawa N. Formation of ultrahigh density and ultrasmall coherent beta-FeSi$_2$ nanodots on Si (111) substrates using Si and Fe codeposition method. *Journal of Applied Physics* 2006; **100**: 044313–044315.

29. Terasawa S, Inoue T, Ihara M. Fabrication of β-FeSi$_2$/Si composite films for photovoltaic applications by using scanning annealing. *Solar Energy Materials and Solar Cells* 2009; **93**: 215–221.

30. Sun CM, Tsang HK, Wong SP, Cheung WY, Ke N, Hark SK. Rapid thermal annealing of ion beam synthesized beta-FeSi$_2$ nanoparticles in Si. *Applied Physics Letters* 2008; **92**: 211902–1.

31. Roura P, Farjas J, Pinyol A, Bertran E. The crystallization temperature of silicon nanoparticles. *Nanotechnology* 2007; **18**: 175705, 1–4.